Stabilization of the Polar Structure and Giant Second-Order Nonlinear Response of Single Crystal γ-$NaAs_{0.95}Sb_{0.05}Se_2$

Abishek K. Iyer[1#], Jingyang He[2#], Hongyao Xie[1], Devin Goodling[2], Duck-Young Chung[3], Venkatraman Gopalan[2], Mercouri G. Kanatzidis[1*]*

[1] Department of Chemistry, Northwestern University, Evanston, Illinois, 60208, United States
[2] Department of Materials Science and Engineering, Pennsylvania State University, University Park, Pennsylvania, 16802, United States
[3] Materials Science Division, Argonne National Laboratory, 9700 South Cass Avenue, Lemont, IL 60439, United States

# Equal Contribution
* Corresponding Authors

Abstract

The dearth of suitable materials significantly restricts the practical development of infrared (IR) laser systems with highly efficient and broadband tuning. $AgGaQ_2$ (Q = S, Se) and $ZnGeP_2$ are used; however, they present certain limitations. Recently, γ-$NaAsSe_2$ has been reported, and it exhibits a large nonlinear second-harmonic generation (SHG) coefficient of 590 pm V^{-1} at 2 μm. However, the crystal growth of γ-$NaAsSe_2$ is challenging because it undergoes a phase transition to centrosymmetric δ-$NaAsSe_2$. Herein, we report the suppression of the phase transition and stabilization of non-centrosymmetric γ-$NaAsSe_2$ by doping the As site with Sb, which results in γ-$NaAs_{0.95}Sb_{0.05}Se_2$. The congruent melting behavior of γ-$NaAs_{0.95}Sb_{0.05}Se_2$ is confirmed by differential thermal analysis at a melting point of 450 °C and crystallization temperature of 415 °C. Single crystals with dimensions of (3 mm × 2 mm) were successfully obtained via zone refining and the Bridgman method. The purification of the material plays a significant role in crystal growth and results in a bandgap of 1.78 eV. The thermal conductivity of γ-$NaAs_{0.95}Sb_{0.05}Se_2$ exhibits a low value of 0.78 W m^{-1} K^{-1} at room temperature, which is lower than that of the three commercially used IR materials. The single-crystal SHG coefficient of γ-$NaAs_{0.95}Sb_{0.05}Se_2$ exhibits an enormous value of $|d_{11}|$ = 648 ± 74 pm V^{-1}, which is comparable to that of γ-$NaAsSe_2$ and approximately 20 times larger than that of $AgGaSe_2$. The bandgap of γ-$NaAs_{0.95}Sb_{0.05}Se_2$ (1.78 eV) is similar to that of $AgGaSe_2$, thus rendering it highly attractive as a high-performing nonlinear optical material.

Key words: polymorphic transitions, chalcogenides, crystal, SHG

1. Introduction

Infrared (IR) high-performing nonlinear optical (NLO) materials are essential for various applications, such as environmental monitoring and imaging devices.[1] Unlike oxides, chalcogenides and phosphides function well in the 2–20 μm range as they are optically transparent in this region.[2, 3] Currently, only three materials, $AgGaS_2$, $AgGaSe_2$, and $ZnGeP_2$, are used commercially for applications in the 2–20 μm range.[4] Reviews by Liang et al.[5], Li et al.[6] and Chung et al.[7] highlighted numerous chalcogenides, most of which were characterized by powder second-harmonic generation (SHG) measurements. Powder SHG measurements are useful for initial testing to obtain the average SHG response of the material and provide a valuable guide for large crystal growth.[8] Luo et al. highlighted the recent progress and challenges in the growth of promising single-crystal chalcogenides, such as $BaGa_4Se_7$ and $Li_2In_2GeSe_6$.[9] We recently reported that the single-crystal γ-$NaAsSe_2$ exhibit an SHG coefficient of d_{11} = 590 ± 51 pm V^{-1}, measured at wavelengths above 2 μm.[10] However, γ-$NaAsSe_2$ undergoes a polymorphic phase transition to centrosymmetric (CS) δ-$NaAsSe_2$ near its melting point, complicating its crystal growth.[10-11]

Wu et al. discussed non-centrosymmetric (NCS) chalcogenides undergoing polymorphic transitions, wherein the NCS structure transitions to an NCS polymorph or CS polymorphs;[12] they reported that all phase transitions hinder the crystal growth process and significantly affect the quality of crystals. As summarized in Table 1, γ-$NaAsSe_2$ (d_{11} = 590 ± 51 pm V^{-1}, i.e., approximately 18 times larger than $AgGaSe_2$)[10] is a high-performing chalcogenide NLO material in the IR region. The bandgap of γ-$NaAsSe_2$ (1.87 eV) is comparable to that of $AgGaSe_2$, and it has a much lower melting point (450 °C) than that of $AgGaSe_2$ (950 °C). The high SHG coefficient value, relatively wide bandgap, and low melting and crystallization temperatures render γ-$NaAsSe_2$ highly attractive as an NLO material. We attempted to stabilize the γ-phase by cation substitution with Li and K without success. $Li_{0.2}Na_{0.8}AsSe_2$ undergoes a phase transition to the δ-phase,[11] whereas $Na_{0.2}K_{0.8}AsSe_2$ melts congruently but shows a significantly low SHG response (approximately 0.8 times larger than that of $AgGaSe_2$).[13] Attempts to stabilize the γ-phase by substituting Na with Ag or Se with S and Te were also unsuccessful. In a recent review the role of chemical substitution in other NC chalcogenide systems has been highlighted.[14]

Recently, we reported the stabilization of NCS β-$LiAsSe_2$ by substituting Se with S, which resulted in the suppression of the phase transition of $LiAsSe_{1.75}S_{0.25}$.[15] In this study, we successfully stabilized the desired γ-phase by substituting 5 % of As with Sb. Successful crystal growth using the Bridgman method was achieved after purification via zone refining, thus resulting in better quality crystals. The SHG coefficient of this material was 648 ± 71 pm V^{-1}, the highest value among semiconductors with a bandgap greater than 1.5 eV.

2. Experimental Details

Synthesis and characterization of γ-$NaAs_{0.95}Sb_{0.05}Se_2$

Reagents: All manipulations were performed in a glove box in a dry nitrogen atmosphere. Commercially available sodium (Na, Sigma-Aldrich, 99.5 %, 2N), arsenic (As, Alfa Aesar, 99.999 %, 5N), antimony (Sb, Alfa Aesar, 99.999 %, 5N), and selenium (Se, American Elements, 99.999 %, 5N) were used without further purification. Na_2Se was prepared via a modified procedure previously reported in the literature by reacting sodium and selenium in liquid ammonia.[16] *Warning: Elemental arsenic is highly toxic and must always be weighed in a glove box in an inert atmosphere, and precautions must be taken when preparing these samples.*

Synthesis of polycrystalline γ-$NaAs_{0.95}Sb_{0.05}Se_2$: First, 5 g of γ-$NaAs_{0.95}Sb_{0.05}Se_2$ was synthesized by combining 1.2098 g Na_2Se (9.68 mmol), 1.378 g As (18.39 mmol), 0.117 g Sb (0.960 mmol), and 2.293 g Se (29.04 mmol) Se. This mixture was thoroughly ground in the glove box and loaded in a separate carbon-coated fused-silica tube (outer diameter (OD): 13 mm). Carbon-coated fused-silica tubes were used to prevent the reaction of the tube with the alkali metal. Subsequently, the tube was flame-sealed under vacuum (approximately 3×10^{-3} mbar) and inserted into a single-zone programmable vertical tube furnace. For the reaction to proceed, the temperature programming of the furnace was as follows. The temperature increased to 610 °C over 10 h, annealed for 36 h, and cooled to 300 °C over 48 h, at which point the furnace was turned off. Grey-colored ingots were obtained after the reaction and produced a red-colored powder upon grinding. Figure 1a shows the powder X-ray diffraction (PXRD) patterns, which confirm the phase and phase purity of the synthesized compound. The composition was confirmed using scanning electron microscopy-energy dispersive X-ray (SEM-EDX) analysis. The SEM-EDX results reveal a uniform composition of $NaAs_{0.92}Sb_{0.10}Se_2$ (Figure S1a), averaged over 15 spots on a single crystal, as shown in Figure S1b. The single-crystal refinement data for γ-$NaAs_{0.95}Sb_{0.05}Se_2$ is

presented in Table S1, the atomic coordinates in Table S2, anisotropic atomic displacement values in Table S3, and selected bond lengths in Table S4.

Bridgman crystal growth method for γ-$NaAs_{0.95}Sb_{0.05}Se_2$: First, 20 g of the as-synthesized ingot was passed through a zone refining system with eight passes. Subsequently, the ends of the resulting ingot (Figure S2) were removed, and it was transferred into a carbon-coated conical-tipped fused-silica tube (inner diameter (ID): 10 mm; OD: 13 mm) and flame-sealed under vacuum (approximately 3×10^{-3} mbar). The sealed ampoule was placed inside a vertical two-zone Bridgman furnace to grow a large single crystal of γ-$NaAs_{0.95}Sb_{0.05}Se_2$. First, the ampoule was kept in the upper hot zone of the Bridgman furnace at 610 °C for 12 h to ensure the thorough melting of the ingot. Subsequently, the ampoule was translated from the upper hot zone to the lower cold zone (350 °C) at a rate of 1 mm h^{-1}. After crystallization was complete, the ampoule was held inside the cold zone (350 °C) for 60 h and finally dropped to room temperature at 10 mm h^{-1}.

Thermal conductivity measurements: The γ-$NaAs_{0.95}Sb_{0.05}Se_2$ crystals were crushed and ground into a fine powder, and sintered in a spark plasma sintering (SPS) apparatus at 523 K under a pressure of 40 MPa in vacuum for 5 min to obtain a dense bulk sample (j = 12.7 × 6.5 mm, density = 3.9033 g cm^{-3}). The sintered sample was cut and polished into two 6 × 6 × 1.5 mm pieces for thermal diffusivity measurement. One of the two pieces was perpendicular to the SPS pressing direction, whereas the other was in the parallel direction. Thermal conductivity was calculated using the thermal diffusivity (D), heat capacity (C_p), and sample density (r) according to the relationship $k = DC_pr$. Thermal diffusivity was measured in an Ar atmosphere using the laser flash method (LFA 457; NETZSCH). The heat capacity (0.3858 J g^{-1} K^{-1}) was calculated using the Dulong–Petit law, and the sample density was determined by measuring the mass and dimensions of the sample.

***Spectroscopic ellipsometry*:** Spectroscopic ellipsometry was performed using a Woollam M-2000F focused beam spectroscopic ellipsometer. The measurements were performed on three crystal orientations: a) [001]// lab Z, [010]// lab X, b) [001] // lab Z, [010] // lab Y, and c) [010]// lab Z, [001]// lab X. The three sets of ellipsometry data were simultaneously fitted to Tauc–Lorentz oscillator model, each of which included an amplitude (A_m), full width at half-maximum (FWHM, B_m), energy center ($E_{0,m}$), and Tauc gap ($E_{g,m}$), as listed in Table S5.

SHG measurements: SHG experiments were performed using a fundamental laser beam generated using an optical parametric amplification (OPA) system pumped by the Ti: sapphire laser system (Spectra-Physics, OPA-800C) with an operating wavelength of 3 μm, repetition rate of 1 kHz, and pulse width of 100 fs. The beam was linearly polarized, and its polarization direction (ψ) was rotated by 360° using a half-wave plate. The second-harmonic beam generated was separated from the fundamental beam using a dichroic mirror, decomposed into *p*- and *s*-polarized components, and collected by a photomultiplier tube (PMT) detector. A wedged X-cut $LiNbO_3$ crystal (MTI Corporation) was used as the reference to obtain the absolute SHG coefficient.

3. Result and Discussion

γ-$NaAs_{0.95}Sb_{0.05}Se_2$ was synthesized by combining Na_2Se or Na, As, Sb, or Se at 550 °C, which crystallized in the monoclinic polar space group, *Pc*. The parent compound $NaAsSe_2$ crystallized in two polymorphs: NCS γ-$NaAsSe_2$, which was obtained by cooling at 10 °C h^{-1}, and δ-$NaAsSe_2$, which was formed by flame melting followed by water quenching or remelting of γ-$NaAsSe_2$. In a previous study, we reported the crystal growth of γ-$NaAsSe_2$ using the Bridgman method, with a slow translational speed of 0.5 mm h^{-1}.[10] However, large, high-quality single crystals could not be obtained because of the phase transition of γ-$NaAsSe_2$ to δ-$NaAsSe_2$ near the melting point (450 °C).

The γ-$NaAsSe_2$ structure had four Na, four As, and eight Se crystallographic sites. Previous investigations on alkali cation substitution of the Na ion site with Li ions revealed that $Li_{0.2}Na_{0.8}AsSe_2$[11] could be converted from the γ- to the δ- phase, whereas $Na_{0.2}K_{0.8}AsSe_2$[13] crystallizes only in the δ-phase with CS configuration. The type of phase obtained for various substitutions is summarized in Table 2. Only $NaAs_{0.95}Sb_{0.05}Se_2$, $Li_{0.05}Na_{0.95}AsSe_2$, and $Na_{0.95}Ag_{0.05}AsSe_2$ were formed in the γ-$NaAsSe_2$ phase. The details of the synthesis of all compounds are available in the supporting information (SI). The comparison of PXRD patterns of δ-$NaAsSe_2$ with those of $Na_{0.95}K_{0.05}AsSe_2$, $NaAsSe_{1.95}S_{0.05}$, and $NaAsSe_{1.95}Te_{0.05}$ are shown in Figure S3, and the comparison of $NaAs_{0.95}Sb_{0.05}Se_2$ with the NCS phase is shown in Figure 1a. Figure 1b shows a comparsion pXRD pattern for γ-$NaAsSe_2$ confirming that Sb substitution retains the noncentrosymmetric phase.

Differential thermal analysis (DTA) on γ- $Li_{0.05}Na_{0.95}AsSe_2$ (Figure S4b) and γ-$Na_{0.95}Ag_{0.05}AsSe_2$ (Figure S4d) showed that after melting and solidifying the materials showed a powder pattern

matching δ-$NaAsSe_2$ (Figures S4a and S4c). However, substituting the As sites with Sb in γ-$NaAs_{0.95}Sb_{0.05}Se_2$ suppressed its transition to δ-$NaAsSe_2$. Figure 1c shows that the melting point (T_m) of γ-$NaAs_{0.95}Sb_{0.05}Se_2$ was observed to be 450 °C and the crystallization temperature (T_c) to be 415 °C, which is similar to that of γ-$NaAsSe_2$ (T_m = 444 °C and T_c = 413 °C).[10, 11] The PXRD pattern of γ-$NaAs_{0.95}Sb_{0.05}Se_2$ before and after DTA was similar, as shown in Figure 1d. The regrinding and melting of the as-synthesized γ-$NaAs_{0.95}Sb_{0.05}Se_2$ in a tube furnace followed by cooling, also confirmed the retention of the NCS γ-phase (Figure S5).

The PXRD data indicate that the γ-$NaAs_{0.95}Sb_{0.05}Se_2$ powder was stable for at least 3 days (Figure S6a) after which surface degradation was observed, whereas the γ-$NaAsSe_2$ powder was typically stable in the air for less than a day (Figure S6b). The stability of γ-$NaAs_{0.95}Sb_{0.05}Se_2$ in the air is essential for crystal processing and polishing. However, both samples were sensitive to a drop of water, and their solutions immediately turned black. The residue obtained after distillation was confirmed to be Se, indicating that special care should be taken during polishing the single crystals. Polishing of γ-$NaAs_{0.95}Sb_{0.05}Se_2$ was successful only using mineral oil and the surface did not degrade when left in air for a day.

Single-crystal diffraction analysis of $NaAs_{0.95}Sb_{0.05}Se_2$ crystal confirmed that it crystallized in the γ-$NaAsSe_2$ structure. The key feature of the γ-$NaAsSe_2$ structure is the one-dimensional (1D) $^1/_\infty[AsQ_2^-]$ chains comprising corner-sharing pyramidal AsQ_3 units. The crystal packing of these chains depends on the atomic radii of alkali metals.[11, 13] Details of the crystal structure of the γ-$NaAsSe_2$ can be found in previous studies.[10, 11, 13] Figure 2 shows the 1D $^1/_\infty[AsQ_2^-]$ chains, highlighting the differences between γ-$NaAs_{0.95}Sb_{0.05}Se_2$ and γ-$NaAsSe_2$. Evidently, γ-$NaAs_{0.95}Sb_{0.05}Se_2$ exhibited two different As sites, one with 100 % As occupancy and the other with As/Sb (M) mixed occupancy, which resulted in slightly different bond lengths. Table 3 lists the terminal (As–Se_t) and bridging (As–Se_b) bond lengths in γ-$NaAsSe_2$, δ-$NaAsSe_2$, and γ-$NaAs_{0.95}Sb_{0.05}Se_2$. As highlighted in Table 3, the As–Se_b bond length in γ-$NaAsSe_2$ (2.51 Å) was greater than that in δ-$NaAsSe_2$ (2.47 Å). Comparatively, the M–Se bond length in γ-$NaAs_{0.95}Sb_{0.05}Se_2$ was 2.55 Å, which indicates that the mixing of Sb in the As site retained the chain conformation by reducing the strain on the M–Se bond. The addition of Sb gives the 1D $^1/_\infty[AsQ_2^-]$ chains more flexibility in comparison to γ-$NaAsSe_2$ where, the chains are rigid and more strained. The increase in M–Se bond length due to the As/Sb site mixing increased the interchain distances along the *c*-axis from those ranging 3.59 Å; 3.63 Å in γ-$NaAsSe_2$ to 3.63 Å;

3.67 Å in γ-$NaAs_{0.95}Sb_{0.05}Se_2$, as shown in Figure 2. Figure S7 highlights the As–Se bond length comparison among γ-$NaAsSe_2$, δ-$NaAsSe_2$, γ-$NaAs_{0.95}Sb_{0.05}Se_2$, and $Na_{0.2}K_{0.8}AsSe_2$, thereby confirming that compounds δ-$NaAsSe_2$ and $Na_{0.2}K_{0.8}AsSe_2$, which do not undergo a phase transition, have similar As–Se bond length.

Coefficient of thermal expansion and thermal conductivity of γ-$NaAs_{0.95}Sb_{0.05}Se_2$

Variable-temperature powder refinements (Figure S8 a-f) were performed to obtain the thermal expansion coefficient and gain insights into the thermal conductivity and expansion behavior of γ-$NaAs_{0.95}Sb_{0.05}Se_2$. Temperature-dependent X-ray refinements of the powder diffraction data were performed using the Jana2006 crystallographic software. We calculated the coefficient of thermal expansion (CTE) using the following equation based on the obtained cell constants.

$$\alpha_l = \frac{\Delta l/\Delta T}{l_0}, \quad (1)$$

where α_l represents the thermal expansion coefficient; Δl represents the change in the unit cell edge length; ΔT represents the change in temperature; and l_0 represents the unit cell edge length at the base temperature of the measurement.[17]

Figure 3a shows the unit cell dimensions (*a*, *b,* and *c*) and the thermal expansion coefficients. The order of the thermal expansion coefficients, α_b (2.1×10^{-5} K^{-1}) > α_a (8.2×10^{-6} K^{-1}) ≈ α_c (5.77×10^{-6} K^{-1}), indicates strong anisotropy of γ-$NaAs_{0.95}Sb_{0.05}Se_2$ along the *b*-axis. Structurally, the interchain direction is along the *c*-axis, and the 1D $^1/_\infty[AsQ_2^-]$ chains are along the *a*-axis. The lengths of the *a*- and *c*-axes were similar, whereas the *b*-axis was much shorter. The longest Na–Se (2.96 Å) and the shortest As–Se bond (2.34 Å) along the *b*-axis lengthened much faster compared with the longer As–Se bonds.

The temperature-dependent thermal conductivity data for γ-$NaAs_{0.95}Sb_{0.05}Se_2$ are shown in Figure 3b. Although the sample sintered via SPS is a polycrystalline material, γ-$NaAs_{0.95}Sb_{0.05}Se_2$ is a monoclinic system and an anisotropic material; thus, the SPS pressure may induce a preferred orientation in the sintered pellet. Thermal conductivity was measured in two directions to understand the thermal transport behavior of γ-$NaAs_{0.95}Sb_{0.05}Se_2$: 1) along the SPS pressing direction, indicated as the *v*-direction (∥), and 2) in a direction perpendicular to the SPS pressing direction, marked as the *p*-direction (⊥, Figure 3b).

Because of the anisotropy of the crystal and the preferred orientation induced by the SPS pressure, the thermal conductivity in the *p*-direction was slightly lower than that in the *v*-direction, as shown

in Figure 3b, which is typical in such anisotropic materials. In Figure S9, the PXRD patterns of the two SPS pellets reveal a preferred orientation along the *p*-direction, which is dominated by the (*00l*) Bragg reflections. Moreover, the sample exhibited an extremely low lattice thermal conductivity of 0.78 W m^{-1} K^{-1} at room temperature and it dropped to 0.41 W m^{-1} K^{-1} at 523 K. Table S7 lists the room temperature thermal conductivity on single crystals of some commonly studied NC chalcogenides. The thermal conductivity of γ-$NaAs_{0.95}Sb_{0.05}Se_2$ at room temperature (0.78 W m^{-1} K^{-1}) is comparable to that of $BaGa_4Se_7$ (0.74 W m^{-1} K^{-1} ∥ c and 0.64 W m^{-1} K^{-1} ⊥ c)[18]. The thermal conductivity of γ-$NaAs_{0.95}Sb_{0.05}Se_2$ is much lower than that of $AgGaS_2$, $AgGaSe_2$, and $ZnGeP_2$, thus rendering it attractive for crystal growth. The thermal conductivity of a polycrystalline sample can be influenced by grain boundary scattering but it should not be very different to a single crystal.[19] Attempts are being made to obtain large single crystals which can offer a full understanding of the intrinsic properties of this γ-$NaAs_{0.95}Sb_{0.05}Se_2$. The ultralow thermal conductivity of γ-$NaAs_{0.95}Sb_{0.05}Se_2$ is attributed to strong phonon-phonon scattering, which may be due to the different bond lengths of the As–Se bonds and point defects arising from the As/Sb site mixing. Figure S10 shows the temperature dependent thermal diffusivity data for γ-$NaAs_{0.95}Sb_{0.05}Se_2$ showing greater thermal diffusion along the *v*-direction compared to the *p*-direction.

4. Crystal growth using the Bridgman method

The as-synthesized materials were loaded into a 13 mm (outer)× 11 mm (inner) diameter carbon-coated tube. Successful crystal growth of γ-$NaAs_{0.95}Sb_{0.05}Se_2$ was achieved using the Bridgman method by translating 20 g of the as-synthesized material at a rate of 1 mm h^{-1}. The PXRD pattern of the sample cleaved from the ingot was obtained to confirm the orientation of the crystal, as shown in Figure 4a. The only observed reflections were those of the (*00l*) family of Bragg reflection. In our initial iterations of crystal growth, we used 3N (99.9%) starting materials, with a hot end at 550 °C and a cold end at 350 °C. The obtained ingot had some hollow spaces, which resulted in poor crystal quality. This could be attributed to small oxide impurities in arsenic or sodium. Figures S11a and S11b show the possible defects in the ingot. Subsequently, we synthesized the material using 5N (99.999%) starting materials by maintaining the hot zone in the Bridgman furnace at 610 °C to observe whether the decreased viscosity minimizes the hollow pockets in the ingot. Figures 11c and 11d show an improved crystal quality; however, the hollow

spaces still existed, although with much smaller pockets. At this point, zone refining of the as-synthesized materials was performed in a carbon-coated fused-silica tube. Horizontal zone refining was performed using eight passes of a narrow heater (12 mm heating zone) at a speed of 5 mm h^{-1} and a temperature of approximately 600 °C. The ingot obtained after this process is shown in Figure S2. Subsequently, the dark-colored material segregated at the top part of the tube was discarded before crystal growth using the Bridgman method. The obtained ingot was significantly improved with fewer hollow spaces. Figure 4b shows the shiny ingot and the cleaved crystal polished using mineral oil. Figure 4c shows that the FWHM was 0.1305 (6) with $\Delta\theta$ = 0.31. However, because of the softness of the crystal, polishing resulted in scratches on the crystal surface (Figure S12). Further efforts are being made to reduce the hollow spaces in the ingot obtained through the purification of the starting materials, which will help grow larger crystals.

5. Linear and nonlinear optical properties of γ-$NaAs_{0.95}Sb_{0.05}Se_2$

Diffuse Reflectance Spectroscopy of γ-$NaAs_{0.95}Sb_{0.05}Se_2$

Figure 5 shows that the bandgap for γ-$NaAs_{0.95}Sb_{0.05}Se_2$ (1.78 eV) from the Tauc plot is comparable to that of γ-$NaAsSe_2$ (1.87 eV). However, a small change was observed in the bandgap of γ-$NaAs_{0.95}Sb_{0.05}Se_2$ when the purity of the material was improved, as shown in Figure S13. Synthesis of γ-$NaAs_{0.95}Sb_{0.05}Se_2$ using 3N starting material resulted in a bandgap of 1.71 eV, which increased to 1.78 eV when 5N starting materials were used. However, a minimal difference was observed at the absorption edge except for the inset in Figure S13, which shows the decrease in the tail, thereby indicating that horizontal zone refining purified γ-$NaAs_{0.95}Sb_{0.05}Se_2$. Single-crystal XRD analysis of the crystal obtained from zone-refining confirmed that no change occurred in Sb composition, indicating that the change in the bandgap of γ-$NaAs_{0.95}Sb_{0.05}Se_2$ was due to purification.

The linear optical behavior of single crystal γ-$NaAs_{0.95}Sb_{0.05}Se_2$

Spectroscopic ellipsometry was performed to study the linear optical properties of γ-$NaAs_{0.95}Sb_{0.05}Se_2$ and to extract the complex refractive indices in the 0.2–1 μm wavelength range. Because γ-$NaAs_{0.95}Sb_{0.05}Se_2$ belongs to the monoclinic point group (*m*), its three coordinate systems (namely, the crystallographic coordinates (*a*, *b*, *c*), crystal-physics coordinates (Z_1, Z_2, Z_3), and principal Eigen coordinates (Z_1^e, Z_2^e, Z_3^e)) do not coincide with each other, as shown in Figure 6a. The crystallographic coordinates are Z_2 // *b*, Z_3 // *c*, and Z_1 // $Z_2 \times Z_3$. The principal

coordinates (Z_2^e // Z_2) were obtained by rotating the crystal-physics axes about Z_2 until the dielectric tensor was diagonalized. The angle between the crystal-physics and principal coordinates is defined as α. The ellipsometry data were collected for the three crystal orientations and fitted simultaneously to the Tauc–Lorentz oscillator model to extract the dielectric tensor and complex refractive indices ($\tilde{n}$) in the crystal-physics coordinates, as follows.

$$\tilde{\varepsilon} = \tilde{n}^2 = \begin{pmatrix} \tilde{n}_{11} & 0 & \tilde{n}_{13} \\ 0 & \tilde{n}_{22} & 0 \\ \tilde{n}_{13} & 0 & \tilde{n}_{33} \end{pmatrix}^2 . \quad (2)$$

The complex refractive indices are shown in Figure 6b. The fitting revealed that n_{13} had a negligible value, which might be because the crystal had a near 90° unit cell β angle and is optically orthorhombic, similar to that of the undoped γ-$NaAsSe_2$.[10] The crystals were also investigated using a polarizing microscope with a pair of cross-polarizers. A crystal with a surface normal [010] was rotated from the [001] axis to obtain minimal light intensity. The angle at the minimal light intensity was to be $|\alpha| \leq 0.75°$.

The real parts of the refractive indices of γ-$NaAs_{0.95}Sb_{0.05}Se_2$ in the 750–1000 nm range were fitted using the Cauchy equation[20]:

$$n = \mathrm{A} + \frac{\mathrm{B}}{\lambda^2} + \frac{\mathrm{C}}{\lambda^4} + \frac{\mathrm{D}}{\lambda^6}, \quad (3)$$

and extrapolated to 3 μm because the dispersion is generally small at lower photon energies. Table 4 lists the parameters of the Cauchy equation.

The nonlinear optical behavior of single crystal γ-$NaAs_{0.95}Sb_{0.05}Se_2$

Subsequently, we investigated the second-order NLO properties of γ-$NaAs_{0.95}Sb_{0.05}Se_2$. In SHG, two photons of the same frequency (ω) are combined into a single photon of twice the frequency when they travel through the NLO crystal. The relationship between the induced polarization and incident electric field is $P_{i,2\omega} \propto d_{ijk} E_{j,\omega} E_{k,\omega}$, where d_{ijk} is the second-order optical susceptibility tensor;, and i, j, and k correspond to the polarization directions of the relevant fields.

The SHG effect was studied using optical SHG polarimetry (Figure 7a). The wavelength of the fundamental light (3 μm) and the SHG (1.5 μm) were selected to ensure that the energies of the fundamental light and SHG were below the bandgap. Thus, the SHG process involved only virtual states and was non-resonant. The experiment was performed in reflection geometry at normal incidence. The SHG intensities were measured while the linearly polarized incident beam was rotated by angle ψ. The SHG tensor of γ-$NaAs_{0.95}Sb_{0.05}Se_2$ in Voigt notation can be expressed as:

$$d = \begin{pmatrix} d_{11} & d_{12} & d_{13} & 0 & d_{15} & 0 \\ 0 & 0 & 0 & d_{24} & 0 & d_{26} \\ d_{31} & d_{32} & d_{33} & 0 & d_{35} & 0 \end{pmatrix}. \quad (4)$$

At normal incidence, the d_{eff} can be written as:

$$d_{eff} = (d_{11} t_{\parallel}^2 \cos^2\psi + d_{12} t_{\perp}^2 \sin^2\psi), \quad (5)$$

when the analyzer was parallel to the Z_1 direction; here, $t_{\parallel}$ and $t_{\perp}$ are the transmission Fresnel coefficients of *p*- and *s*-polarized fundamental light, respectively. The collected polar plot was fitted based on d_{eff}, as shown in Figure 7b. A wedged X-cut $LiNbO_3$ crystal was measured under similar experimental conditions as the reference and compared with γ-$NaAs_{0.95}Sb_{0.05}Se_2$ to extract the absolute value of d_{11}. A comparison of the SHG intensities of γ-$NaAs_{0.95}Sb_{0.05}Se_2$ and $LiNbO_3$ at $\psi = 0°$ revealed that $|d_{11}| = 648 \pm 74$ pm V^{-1}. This experimental geometry would also allow us to probe d_{12}; however, similar to the parent compound γ-$NaAsSe_2$, the large magnitude of d_{11} dominated the polar plot and d_{11}/d_{12} ratio. Hence, only the upper boundary of d_{12} was determined. Evidently, the results revealed that $d_{11}/d_{12} \geq 14$, and thus, $|d_{12}| \leq 45$ pm V^{-1}.

Compared with γ-$NaAsSe_2$, γ-$NaAs_{0.95}Sb_{0.05}Se_2$ exhibited similar linear and nonlinear optical properties. For example, both crystals exhibited a larger SHG response in the [100] direction owing to the alignment and extension of the 1D chains in both crystals along the [100] direction. The SHG coefficient of γ-$NaAs_{0.95}Sb_{0.05}Se_2$ was greater than that of γ-$NaAsSe_2$ likely because of the smaller bandgap.[1, 2] The second-order nonlinearity of γ-$NaAs_{0.95}Sb_{0.05}Se_2$ also surpassed those of commercial NLO crystals and was approximately 20 times higher than that of $AgGaSe_2$ (Figure 7c).[3]

Additionally, we calculated the non-phase-matched SHG conversion efficiency of γ-$NaAs_{0.95}Sb_{0.05}Se_2$ by utilizing the giant d_{11} value and compared it with commercial NLO crystals, such as $LiNbO_3$, $AgGaSe_2$, and $ZnGeP_2$. When the fundamental and SHG waves travel in the material, they interfere with each other and the SHG wave is converted back to the fundamental wave. The SHG intensity has a maximum when the distance traveled by the waves is one coherence length l_c, which is defined as follows.

$$l_c = \frac{\lambda_\omega}{2(n_{2\omega} - n_\omega)}, \quad (6)$$

where $n_{2\omega}$ and n_ω are the refractive indices at frequencies of 2ω and ω, respectively.[21] In Figure 7d the coherence lengths of γ-$NaAs_{0.95}Sb_{0.05}Se_2$ are compared with those of other commercial NLO

crystals when the largest SHG coefficients were used. Evidently, γ -$NaAs_{0.95}Sb_{0.05}Se_2$ exhibited a coherence length comparable to that of $ZnGeP_2$; however, its SHG coefficient was nearly ten times greater. γ-$NaAs_{0.95}Sb_{0.05}Se_2$ has a smaller coherence length than γ-$NaAsSe_2$ because it has a larger refractive index dispersion as seen from equation 6. We expect the coherence length of γ-$NaAs_{0.95}Sb_{0.05}Se_2$ to increase when probing further into the infrared range since the refractive index dispersion will decrease as the wavelength increases.[22] Subsequently, we calculated the SHG conversion efficiency for one coherence length normalized by the fundamental intensity, as follows.

$$\frac{I_{2\omega}}{I_{\omega}^2} = \frac{2\omega^2}{\varepsilon_0 c^3}\frac{d^2}{n_{2\omega}{n_\omega}^2}\frac{1}{l_c}\int_0^{l_c} l^2 \mathrm{sinc}^2\left(\frac{\Delta k l}{2}\right) dl, \quad (7)$$

where ε_0 is the vacuum permittivity; c is the light velocity; and Δk is the wave vector difference between the fundamental and SHG waves. Figure 7e shows the non-phase-matched SHG conversion efficiency for the largest SHG coefficients of γ-$NaAs_{0.95}Sb_{0.05}Se_2$, $LiNbO_3$, $AgGaSe_2$, and $ZnGeP_2$.[23] At a fundamental wavelength of 2.5 μm γ-$NaAs_{0.95}Sb_{0.05}Se_2$ was almost 100 times more efficient than $ZnGeP_2$.

Similar to γ-$NaAsSe_2$, γ-$NaAs_{0.95}Sb_{0.05}Se_2$ is soluble in polar solvents and possesses a chain-like structure that allows easy solution processing of the films. Hence, γ-$NaAs_{0.95}Sb_{0.05}Se_2$ is a good candidate for NLO thin film devices. Considering the large d_{11} value, γ-$NaAs_{0.95}Sb_{0.05}Se_2$ is also an excellent material for orientation-patterned quasi-phase-matched devices.[24]

6. Conclusions

γ-$NaAsSe_2$ is a high-performing NLO material in the mid-infrared (MIR) above 2 μm, and it undergoes a polymorphic phase transition to CS δ-$NaAsSe_2$. Herein, we effectively stabilized γ-$NaAsSe_2$ by substituting it with 5 % Sb which reduces the strain on the 1D $^1/_\infty[AsQ_2^-]$ chains. Single crystals of γ-$NaAs_{0.95}Sb_{0.05}Se_2$ (>2 mm) were successfully grown using the Bridgman growth method. Further crystal growth and processing improvements will render γ-$NaAs_{0.95}Sb_{0.05}Se_2$ highly attractive for high-power laser applications. The linear and nonlinear optical properties were measured and indicated a giant second-order nonlinearity with an optical SHG coefficient of $|d_{11}|$ = 648±74 pm V^{-1}, which is comparable to that of γ-$NaAsSe_2$. With a bandgap comparable to commercial $AgGaSe_2$ but a giant SHG coefficient value, γ-$NaAs_{0.95}Sb_{0.05}Se_2$ is a promising candidate for obtaining infrared lasers.

Associated Content

Supporting Information

Experimental methods and physical property measurements; X-ray crystallographic Tables of the atomic coordinates, displacement parameters, selected bond lengths of γ-$NaAs_{0.95}Sb_{0.05}Se_2$, Table presenting the parameters for linear optical properties, cell constants obtained from temperature-dependent XRD analysis, comparison of thermal conductivity of some commercially attractive materials, SEM-EDAX of single crystal of γ-$NaAs_{0.95}Sb_{0.05}Se_2$; PXRD patterns obtained of all the synthesized materials; DTA of $Li_{0.05}Na_{1.95}AsSe_2$ and $Na_{0.05}Ag_{0.05}AsSe_2$; PXRD patterns of $Li_{0.05}Na_{1.95}AsSe_2$ and $Na_{0.05}Ag_{0.05}AsSe_2$ before and after DTA; PXRD of γ-$NaAs_{0.95}Sb_{0.05}Se_2$ and γ-$NaAsSe_2$ after air stability study, images of the different ingots obtained from Bridgman method; polished crystals of γ-$NaAs_{0.95}Sb_{0.05}Se_2$; X-ray powder refinements of of γ-$NaAs_{0.95}Sb_{0.05}Se_2$; thermal diffusivity of γ-$NaAs_{0.95}Sb_{0.05}Se_2$; optical absorption data of all the synthesized materials of γ-$NaAs_{0.95}Sb_{0.05}Se_2$; linear optical data of γ-$NaAs_{0.95}Sb_{0.05}Se_2$.

The CIF files for the reported compounds can be found in the CSD. The numbers corresponding to these structures are as follows.

CSD number for of γ-$NaAs_{0.95}Sb_{0.05}Se_2$: 2211756

Author Information

* Corresponding authors

Mercouri G. Kanatzidis

E-mail: m-kanatzidis@northwestern.edu

Venkatraman Gopalan

E-mail: vxg8@psu.edu;

Note: The authors declare no competing financial interest.

Acknowledgments

A.K.I, J.H., D.G., V.G., and M.G.K. acknowledge the Air Force Office of Scientific Research Grant number FA9550-18-S-0003. J.H. also received partial support from the National Science Foundation through the Penn State 2D Crystal Consortium-Materials Innovation Platform (2DCC-MIP) under NSF cooperative agreement DMR-2039351. The IMSERC PCM facility at Northwestern University used in this work received support from the Soft and Hybrid Nanotechnology Experimental (SHyNE) Resource (NSF ECCS-2025633). DYC acknowledges that the work at Argonne (material purification and crystal growth) was supported by the U.S. Department of Energy, Office of Science, Basic Energy Sciences, Materials Sciences, and Engineering Division. Scientific discussions and advice from Gary Cook, Carl M. Liebig, Ryan K. Feaver, and Sean A. McDaniel of the Air Force Research Laboratory (AFRL) are gratefully acknowledged. A. K. I. and J.H. contributed equally to this work.

Tables

Table 1: Some reported high-performing chalcogenide NLO materials

Polymorph	Phase transition	Space group	Bandgap (eV)	SHG intensity	Reference
$LiAsSe_2$	α ⟶ β (@ 470 °C)	α = *F*-43*m*; β = *Cc*	α = 1.10; β = 1.11	d_{eff} = 55.7 pm V^{-1}, Theoretical d_{33} = 836.5 pm V^{-1}, 387 pm V^{-1}	[11, 15]
$NaAsSe_2$	γ ⟶ δ (@ 450 °C)	γ = *Pc*; δ = *Pbca*	γ = 1.75; δ = 1.71	γ = 75x $AgGaSe_2$	[10, 11]
$CsPSe_6$	β ⟶ α (@ 273 °C)	α = *P*2/*n*; β = *P*-42$_1$*c*	α = 2.1; β = 1.9	β = 29.6 pm V^{-1},	[25]
$K_2P_2Se_6$	α ⟶ β	α = *P*3$_1$2$_1$; β = *P*3$_1$, glassy	α = 2.1; Glassy: 1.97		[26]
Li_3PS_4	α ⟶ γ (@ 300 °C) γ ⟶ β (@ 227 °C) β ⟶ α (@ 473 °C)	α = *Pbcn*; β = *Pnma*; γ = *Pnm*2$_1$	γ = 3.68	γ = 4.32 pm V^{-1},	[27]
$NaSbP_2S_6$	α ⟶ β	α = *P*2$_1$/*c*; β = *P*2$_1$	α = 2.17; β = 2.25	β = 3×$AgGaS_2$	[28]
$LaGaS_3$	α ⟶ β	α = *P*2$_1$/*c*; β = *Pna*2$_1$	α = 2.50; β = 1.90	Weak SHG	[29]
$Na_2Ge_2Se_5$	α ⟶ β (@500 °C)	α = *Cmcm*; β = *Pna*2$_1$	β = 2.38	290 pm V^{-1},	[30]

Table 2: Phase obtained after substitution in γ-$NaAsSe_2$ and the phase obtained from differential thermal analysis (DTA)

Composition	Phase	Phase after DTA
$Li_{0.05}Na_{0.95}AsSe_2$	γ-$NaAsSe_2$	δ-$NaAsSe_2$
$Na_{0.95}K_{0.05}AsSe_2$	δ-$NaAsSe_2$	Not performed
$Na_{0.95}Ag_{0.05}AsSe_2$	γ-$NaAsSe_2$	δ-$NaAsSe_2$
$NaAs_{0.95}Sb_{0.05}Se_2$	γ-$NaAsSe_2$	γ-$NaAsSe_2$
$NaAsSe_{1.95}S_{0.05}$	δ-$NaAsSe_2$	Not performed
$NaAsSe_{1.95}Te_{0.05}$	δ-$NaAsSe_2$	Not performed

Table 3: As–Se bond length comparison of γ-$NaAsSe_2$, γ-$NaAs_{0.95}Sb_{0.05}Se_2$, and δ- $NaAsSe_2$

As-Se Bond	γ-$NaAsSe_2$	γ-$NaAs_{0.95}Sb_{0.05}Se_2$	δ- $NaAsSe_2$
Bridging	As-Se_b 2.51 Å, 2.46 Å	M-Se_b 2.55 Å, 2.49 Å	As-Se_b 2.47 Å, 2.45 Å
	As-Se_b 2.47 Å, 2.43 Å	As-Se_b 2.49 Å, 2.45 Å	
Terminal	As-Se_t 2.32 Å	M-Se_t 2.36 Å	As-Se_t 2.29 Å
	As-Se_t 2.30 Å	As-Se_t 2.30 Å	

Table 4: Parameters of the Cauchy equations[20] for refractive indices of γ-$NaAs_{0.95}Sb_{0.05}Se_2$ in the 750–1000 nm range in the crystal-physics coordinate.

	A	B	C	D
n_{11}	2.739	0.3056	–0.1295	0.04653
n_{22}	2.273	0.2078	–0.1024	0.03096
n_{33}	2.299	0.2228	–0.1059	0.03298

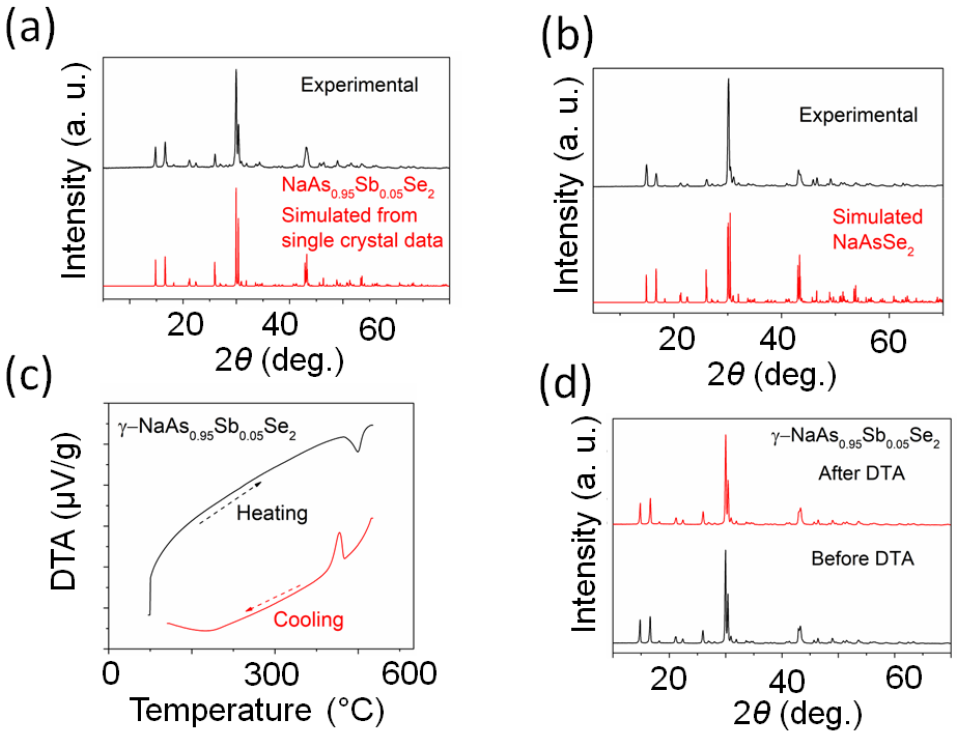

Figure 1: (a) Experimental powder X-ray diffraction (PXRD) patterns of the γ-$NaAs_{0.95}Sb_{0.05}Se_2$ (red) compared with the simulated PXRD patterns from the single crystal of γ-$NaAs_{0.95}Sb_{0.05}Se_2$ (black). (b) Experimental powder X-ray diffraction (PXRD) patterns of the γ-$NaAsSe_2$ (red) compared with the simulated PXRD patterns from the single crystal of γ-$NaAsSe_2$ (c) Differential thermal analysis of γ-$NaAs_{0.95}Sb_{0.05}Se_2$ showing melting (Tm, endothermic, black) and crystallization (Tc, exothermic, red) points. (c) Comparison of the PXRD patterns before (red) and after (black) differential thermal analysis.

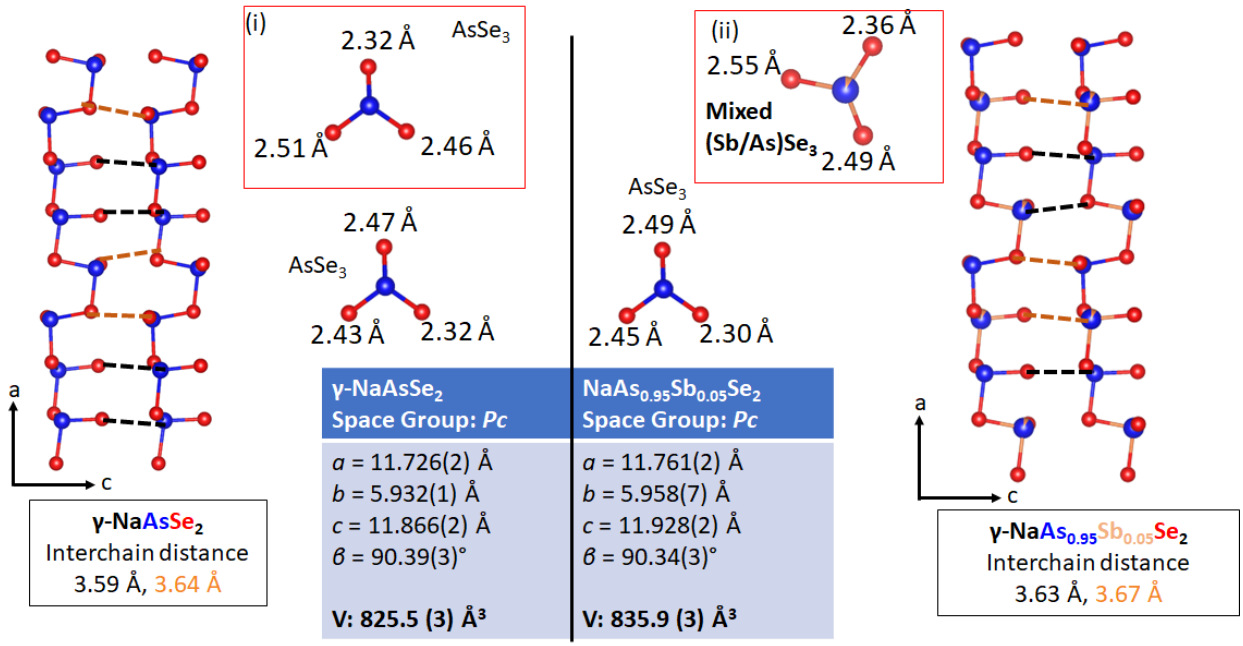

Figure 2: Interchain distances for (a) γ-$NaAsSe_2$ and (b) γ-$NaAs_{0.95}Sb_{0.05}Se_2$ highlighting the increased chain distance in γ-$NaAs_{0.95}Sb_{0.05}Se_2$. (i) $AsSe_3$ bond lengths; (ii) MSe_3 bond lengths (M = As/Sb mixed site) in γ-$NaAs_{0.95}Sb_{0.05}Se_2$.

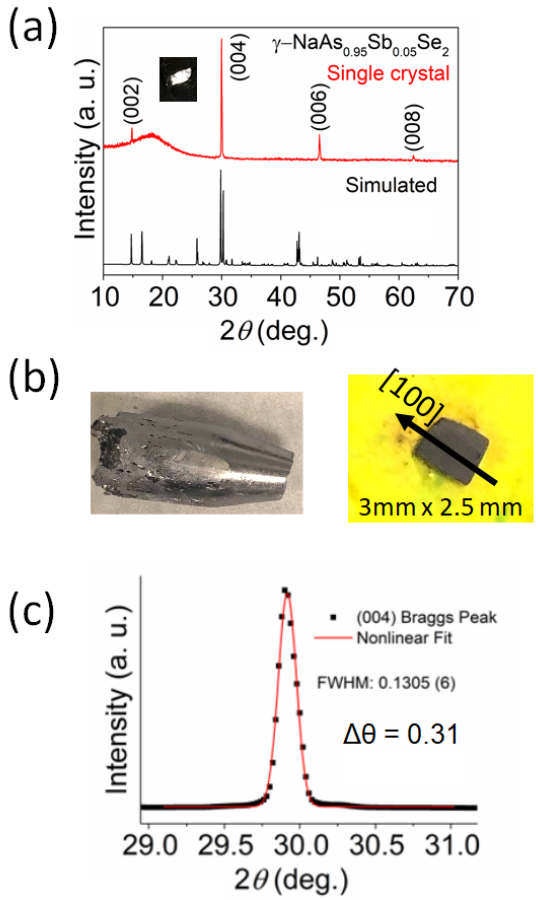

Figure 3: (a) (*00l*) family of Braggs reflection obtained from a cleaved crystal of γ-$NaAs_{0.95}Sb_{0.05}Se_2$. (b) Bridgman ingot obtained from zone refining and the cleaved crystal along the [100] obtained after polishing. (c) (004) Braggs reflection peak fitted with a Gaussian function.

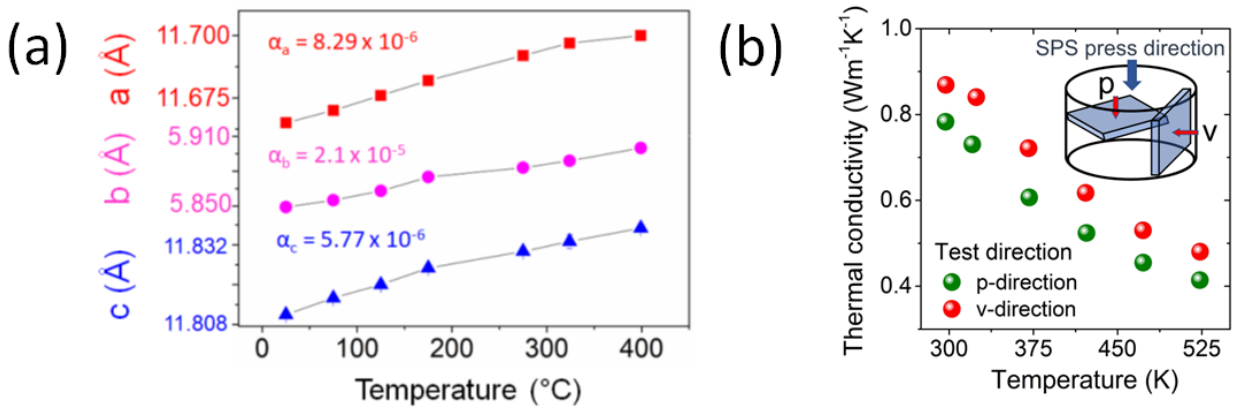

Figure 4: (a) Cell constants (*a*-axis, red; *b*-axis, magenta; *c*-axis, blue) for γ-$NaAs_{0.95}Sb_{0.05}Se_2$ obtained from Le Bail fit; (b) Temperature dependence of the thermal conductivity for γ-$NaAs_{0.95}Sb_{0.05}Se_2$.Because the γ-$NaAs_{0.95}Sb_{0.05}Se_2$ is anisotropic, thermal conductivity is measured in two different directions: one is along the SPS pressing direction, indicated as the *v*-direction, and the other is perpendicular to the SPS pressing direction, which is marked as the *p*-direction.

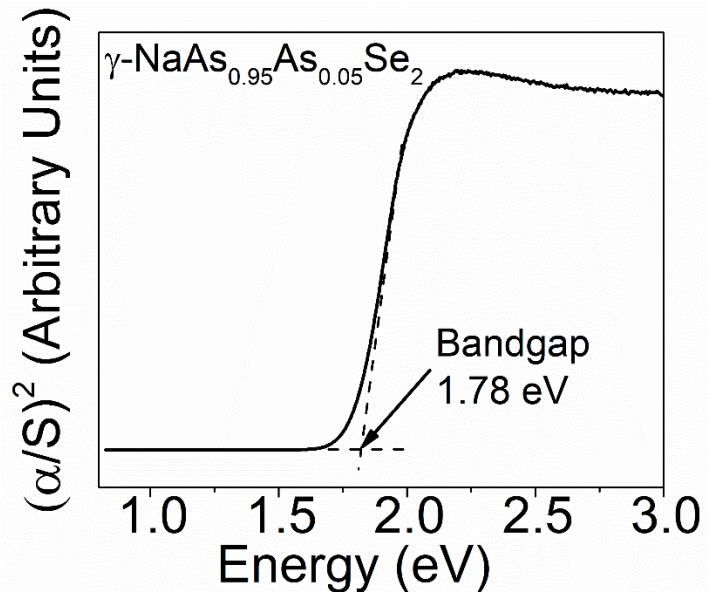

Figure 5: UV–Visible spectrum of γ-$NaAs_{0.95}Sb_{0.05}Se_2$ as obtained from the Tauc plot.

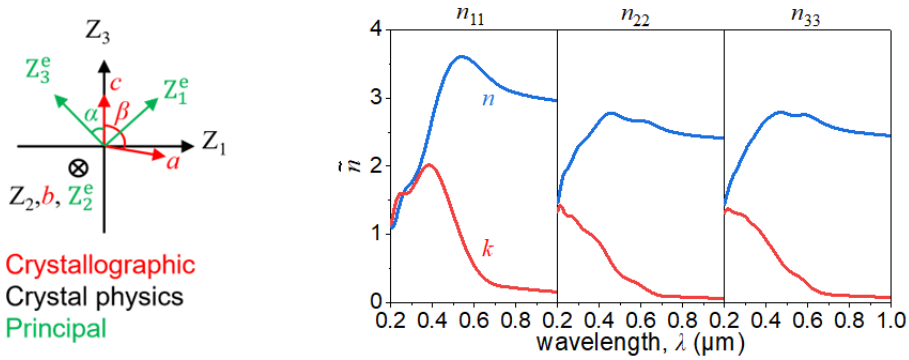

Figure 6: (a) Definitions of the three coordinate systems for γ-$NaAs_{0.95}Sb_{0.05}Se_2$. (b) Complex refractive indices of γ-$NaAs_{0.95}Sb_{0.05}Se_2$ in the visible range. The real and imaginary parts are shown in blue and red, respectively.

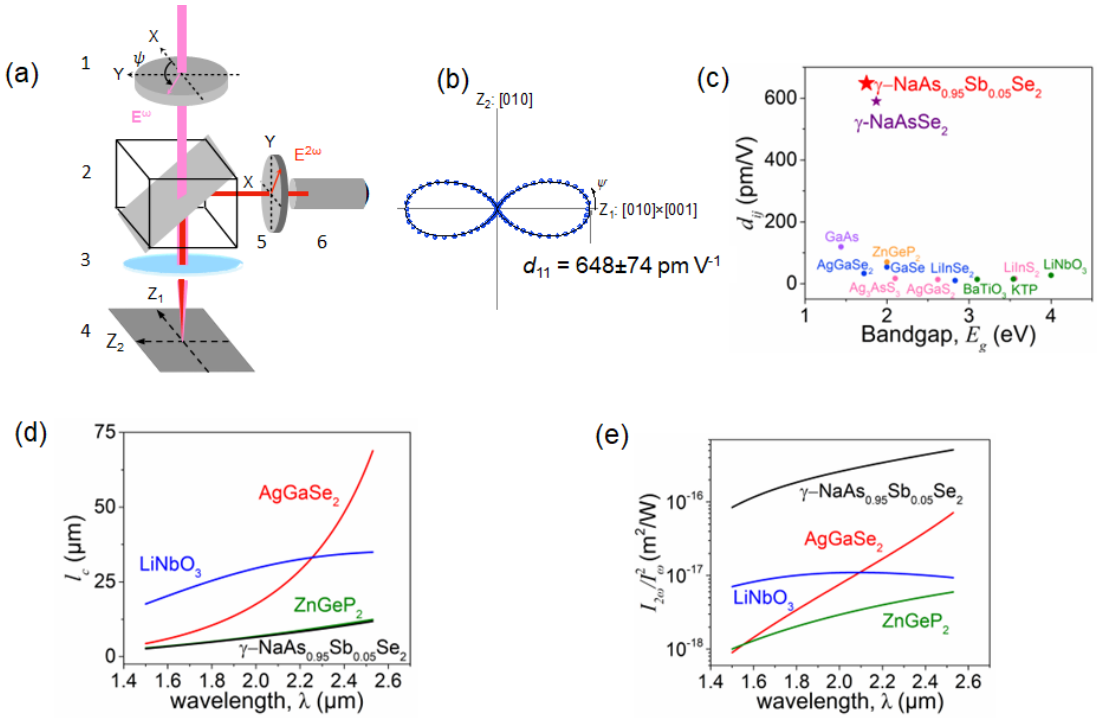

Figure 7: (a) Schematics of the experimental setup, including: 1) half-wave plate, 2) dichroic mirror, 3) lens, 4) sample, 5) analyzer, and 6) detector. (b) Polar plot of the SHG intensities of γ-$NaAs_{0.95}Sb_{0.05}Se_2$ with polarization parallel to the lab X direction. (c) Comparison of the highest SHG coefficients of γ-$NaAs_{0.95}Sb_{0.05}Se_2$, γ-$NaAsSe_2$ and some well-known NLO crystals.[10, 22] (d) Coherence lengths, and (e) non-phase-matched SHG conversion efficiency of $NaAs_{0.95}Sb_{0.05}Se_2$ and the commercial NLO crystals.

References

[1] a) D. Cotter, R. J. Manning, K. J. Blow, A. D. Ellis, A. E. Kelly, D. Nesset, I. D. Phillips, A. J. Poustie, D. C. Rogers, *Science* **1999**, 286, 1523; b) M. Ebrahim-Zadeh, G. Leo, I. Sorokina, *J. Opt. Soc. Am. B* **2018**, 35, MIC1; c) V. A. Serebryakov, É. V. Boĭko, N. N. Petrishchev, A. V. Yan, *J. Opt. Technol.* **2010**, 77, 6; d) M. B. Pushkarsky, I. G. Dunayevskiy, M. Prasanna, A. G. Tsekoun, R. Go, C. K. Patel, *Proc Natl Acad Sci U S A* **2006**, 103, 19630.

[2] J. D. Bierlein, H. Vanherzeele, *J. Opt. Soc. Am. B* **1989**, 6, 622.

[3] G. D. Boyd, R. C. Miller, K. Nassau, W. L. Bond, A. Savage, *Applied Physics Letters* **1964**, 5, 234.
[4] a) A. Harasaki, K. Kato, *Japanese Journal of Applied Physics* **1997**, 36, 700; b) G. C. Catella, L. R. Shiozawa, J. R. Hietanen, R. C. Eckardt, R. K. Route, R. S. Feigelson, D. G. Cooper, C. L. Marquardt, *Appl. Opt.* **1993**, 32, 3948; c) G. D. Boyd, E. Buehler, F. G. Storz, *Applied Physics Letters* **1971**, 18, 301.
[5] F. Liang, L. Kang, Z. Lin, Y. Wu, *Crystal Growth & Design* **2017**, 17, 2254.
[6] Z. Li, J. Yao, Y. Wu, *Crystal Growth & Design* **2020**, 20, 7550.
[7] I. Chung, M. G. Kanatzidis, *Chemistry of Materials* **2014**, 26, 849.
[8] W. Zhang, H. Yu, H. Wu, P. S. Halasyamani, *Chemistry of Materials* **2017**, 29, 2655.
[9] X. Luo, Z. Li, Y. Guo, J. Yao, Y. Wu, *Journal of Solid State Chemistry* **2019**, 270, 674.
[10] J. He, A. K. Iyer, M. J. Waters, S. Sarkar, R. Zu, J. M. Rondinelli, M. G. Kanatzidis, V. Gopalan, *Advanced Optical Materials* **2022**, 10, 2101729.
[11] T. K. Bera, J. I. Jang, J.-H. Song, C. D. Malliakas, A. J. Freeman, J. B. Ketterson, M. G. Kanatzidis, *Journal of the American Chemical Society* **2010**, 132, 3484.
[12] K. Wu, Y. Yang, L. Gao, *Coordination Chemistry Reviews* **2020**, 418, 213380.
[13] A. K. Iyer, J. B. Cho, H. R. Byun, M. J. Waters, S. Hao, B. M. Oxley, V. Gopalan, C. Wolverton, J. M. Rondinelli, J. I. Jang, M. G. Kanatzidis, *Journal of the American Chemical Society* **2021**, 143, 18204.
[14] H. Lin, W.-B. Wei, H. Chen, X.-T. Wu, Q.-L. Zhu, *Coordination Chemistry Reviews* **2020**, 406, 213150.
[15] B. M. Oxley, J. B. Cho, A. K. Iyer, M. J. Waters, J. He, N. C. Smith, C. Wolverton, V. Gopalan, J. M. Rondinelli, J. I. Jang, M. G. Kanatzidis, *Journal of the American Chemical Society* **2022**, 144, 13903.
[16] T. J. McCarthy, M. G. Kanatzidis, *Chemistry of Materials* **1993**, 5, 1061.
[17] N. P. Calta, F. Han, M. G. Kanatzidis, *Inorganic Chemistry* **2015**, 54, 8794.
[18] J. Yao, W. Yin, K. Feng, X. Li, D. Mei, Q. Lu, Y. Ni, Z. Zhang, Z. Hu, Y. Wu, *Journal of Crystal Growth* **2012**, 346, 1.
[19] C. Zhou, Y. K. Lee, Y. Yu, S. Byun, Z.-Z. Luo, H. Lee, B. Ge, Y.-L. Lee, X. Chen, J. Y. Lee, O. Cojocaru-Mirédin, H. Chang, J. Im, S.-P. Cho, M. Wuttig, V. P. Dravid, M. G. Kanatzidis, I. Chung, *Nature Materials* **2021**, 20, 1378.
[20] W. C. Tan, K. Koughia, J. Singh, S. O. Kasap, in *Optical Properties of Condensed Matter and Applications*, DOI: https://doi.org/10.1002/0470021942.ch1 **2006**, p. 1.
[21] S. A. Denev, T. T. A. Lummen, E. Barnes, A. Kumar, V. Gopalan, *Journal of the American Ceramic Society* **2011**, 94, 2699.
[22] G. Chartier, *Introduction to Optics*, Springer New York, **2005**.
[23] D. N. Nikogosyan, *Nonlinear Optical Crystals: A Complete Survey*, Springer, New York, NY **2005**.
[24] K. L. Vodopyanov, O. Levi, P. S. Kuo, T. J. Pinguet, J. S. Harris, M. M. Fejer, B. Gerard, L. Becouarn, E. Lallier, *Opt. Lett.* **2004**, 29, 1912.
[25] A. S. Haynes, A. Banerjee, F. O. Saouma, C. O. Otieno, J. I. Jang, M. G. Kanatzidis, *Chemistry of Materials* **2016**, 28, 2374.
[26] I. Chung, J. I. Jang, C. D. Malliakas, J. B. Ketterson, M. G. Kanatzidis, *J. Am. Chem. Soc.* **2010**, 132, 384.
[27] K. Homma, M. Yonemura, T. Kobayashi, M. Nagao, M. Hirayama, R. Kanno, *Solid State Ionics* **2011**, 182, 53.

[28] a) V. Manríquez, A. Galdámez, D. Ruiz-León, *Materials Research Bulletin* **2006**, 41, 1337; b) L. Kang, M. Zhou, J. Yao, Z. Lin, Y. Wu, C. Chen, *Journal of the American Chemical Society* **2015**, 137, 13049.
[29] P. Li, L.-H. Li, L. Chen, L.-M. Wu, *Journal of Solid State Chemistry* **2010**, 183, 444.
[30] I. Chung, J.-H. Song, J. I. Jang, A. J. Freeman, M. G. Kanatzidis, *J. Solid State Chem.* **2012**, 195, 161.

High performing non-centrosymmetric γ-$NaAsSe_2$ by doping the As site with Sb, which results in γ-$NaAs_{0.95}Sb_{0.05}Se_2$ Single crystals with dimensions of (3 mm × 2 mm) were successfully obtained via zone refining and the Bridgman method. A giant second harmonic generation (SHG) susceptibility of $|d_{11}| = 648 \pm 74$ pm V^{-1} is observed at 2 μm. These properties make it a promising candidate for infrared laser applications.

TOC